

**COMPLEX DRIVERS OF REEF-FRONTED BEACH CHANGE**

A THESIS SUBMITTED TO THE GRADUATE DIVISION OF THE UNIVERSITY  
OF HAWAI‘I AT MĀNOA IN PARTIAL FULFILLMENT OF THE REQUIREMENTS FOR  
THE DEGREE OF

MASTER OF SCIENCE

IN

EARTH AND PLANETARY SCIENCES

DECEMBER 2021

By

Anna Baker Mikkelsen

Thesis Committee:

Charles H. Fletcher, Chairperson

Tiffany R. Anderson

Sloan Coats

**Keywords:** carbonate beach, coastal processes, UAS surveys, environmental monitoring,  
Hawai‘i, self-organizing maps

## ACKNOWLEDGEMENTS

I want to extend my sincerest gratitude to my advisor Dr. Chip Fletcher for your guidance and encouragement through this program. Thank you for patiently teaching me about coastal processes and scientific research while also giving me the flexibility to explore my own paths and interests. Thank you for always encouraging me to achieve my fullest potential. I would also like to thank my committee member Dr. Tiffany Anderson for helping me navigate modelling and statistics. Your countless hours on zoom shaped a large part of the project and introduced me to the intricate details of statistical modelling. Thank you, Dr. Sloan Coats, for your excellent guidance and brainstorming ideas. You provided a different perspective to this project, introduced me to the world of SOMs and assisted with lots of technical troubleshooting. I also want to thank Martin Guilles and Camilla Tognacchini for advice in wave run-up assessments for Waikīkī, Philip Thompson for guidance on sea level change, and Ning Li for insights and helpful discussions about the SWAN nearshore wave model output. Thank you to Kammie Tavares, Noah Kannegiesser, Kristian McDonald, Korey Wong, Catherine Creadick, and Julianne Kalksma for assistance with fieldwork, as well as support and motivation, laughs, many wonderful sunrises at Waikīkī, and most importantly, friendship. From the earth sciences department, thank you Lily and Arlene for your tremendous help in all things paperwork - employment, visas, insurance, purchasing requests and for all the reminders to help us all stay on track. My partner Keo for your love, support, hygge, and for always believing in me. Thanks to Dr. Randy Kosaki, Brain Hauk, and Jason Leonard at PMNM, Jeff Kuwabara, and Dr. Rich Pyle for your (possibly unintentional) excellent mentorship, for believing in me, and allowing me great adventures and great conversations, which eventually led me to this career path – thank you. I would like to thank Kammie Tavares for your laughs, guidance through work and life, showing me around your home and for introducing me to a more holistic science perspective. Thanks also Genevieve and Renee for the many adventures that kept me

Most importantly I would like to thank my family – mom & dad & Bedste. You have always believed in me, whether it was running, moving half a world away, or my academics. You have shown me the world from a young age and supported my dreams, I can only hope that I have made you proud. Thank you.

## ABSTRACT

Royal Hawaiian Beach in Waikīkī plays an essential role in Hawai‘i’s tourism-based economy. To inform development of management policies, we conduct two years of weekly ground and aerial surveys (April 2018 to February 2020) to track change on this chronically eroding beach. We use multiple linear regressions, Self-Organizing Maps (a form of cluster analysis), remotely sensed nearshore sand fields, hydrodynamic modelling, and monitoring of key physical processes to identify the principal drivers of beach change. Our results show 12 months of accretion ( $+2400 \pm 59 \text{ m}^3$ ) followed by 10 months of erosion ( $-3090 \pm 51 \text{ m}^3$ ) for a net loss of  $690 \pm 51 \text{ m}^3$ , and document that interannual variations in beach width and volume overprint seasonal patterns. Notably, a seasonal signal is recorded in the topographic structure of the beach. We test the relationship of beach volume and width to variations in wind, water level, and wave energy flux generated from southern hemisphere swell as well as locally generated trade-wind waves. We identify three beach segments and three nearshore sand fields that form a sand-sharing, source-sink network, yet operate quasi-independently. Our analysis reveals that individual beach segments and their adjacent sand fields experience coherent (simultaneous) gains and losses of sand, suggesting that alongshore sediment exchange is dominant over cross-shore exchange. The main drivers of beach change are variations in water level and wave energy flux. Beach volume and width both vary with nearshore sand cover, indicating that free exchange with nearshore sources is intrinsic to beach variability. Our results suggest that rising sea level and extreme El Niño-Southern Oscillation events will contribute to Royal Hawaiian Beach destabilization, which may amplify erosional events and increase the cost of future beach maintenance.

# TABLE OF CONTENTS

<b>ACKNOWLEDGEMENTS</b> .....	<b>II</b>
<b>ABSTRACT</b> .....	<b>III</b>
<b>LIST OF TABLES</b> .....	<b>VI</b>
<b>LIST OF FIGURES</b> .....	<b>VII</b>
<b>LIST OF ABBREVIATIONS</b> .....	<b>VIII</b>
<b>1. INTRODUCTION</b> .....	<b>1</b>
<b>2. METHODS</b> .....	<b>3</b>
2.1 Field Data.....	4
2.2 Nearshore Sand Cover .....	5
2.3 Self-Organizing Maps (SOMs).....	6
2.4 Physical Variables.....	6
2.5 Multiple Linear Regressions.....	7
<b>3. RESULTS</b> .....	<b>8</b>
3.1 Physical variables .....	8
3.2 Beach observations .....	9
3.2.1 Total beach.....	9
3.2.2 East beach .....	9
3.2.3 Center beach.....	9
3.2.4 West beach.....	10
3.3 Nearshore sand cover.....	11
3.4 Self-Organizing Maps (SOMs).....	12
3.4.1 SOM1 .....	13
3.4.2 SOM2.....	14
3.5 Regression Analysis.....	14
3.5.1 Beach volume.....	16
3.5.2 Beach width .....	17
<b>4. DISCUSSION</b> .....	<b>18</b>
4.1 Trade conditions .....	19
4.2 South swell energy flux .....	19
4.3 Kona storms .....	19
4.4 Quiet conditions .....	20
4.5 Westerly Winds.....	20
4.6 High water levels .....	20
4.7 Differences between segments.....	21
4.8 Profile response.....	21
4.9 Implications for management in a changing climate .....	22
<b>5. CONCLUSIONS</b> .....	<b>24</b>
<b>APPENDIX A: EXTENDED METHODOLOGY</b> .....	<b>25</b>
1. Nearshore Classification.....	25

2. Environmental Variables .....	25
3 Multiple Linear Regression .....	26
3.1 Conditioning environmental variables .....	26
3.2 Eliminating dependent variables .....	27
3.3. Least squares multiple linear regressions .....	27
3.4 Accounting for correlation of model residuals .....	28
3.5 Model averaging .....	29
3.6 Model uncertainty .....	29
<b>APPENDIX B: SUPPLEMENTARY FIGURES.....</b>	<b>31</b>
<b>APPENDIX C: SOURCES OF PHYSICAL ENVIRONMENTAL VARIABLES.....</b>	<b>32</b>
<b>REFERENCES.....</b>	<b>33</b>

**LIST OF TABLES**

Table 1 ..... 15  
Table 2 ..... 18

## LIST OF FIGURES

Figure 1.....	2
Figure 2.....	5
Figure 3.....	7
Figure 4.....	10
Figure 5.....	11
Figure 6.....	13
Figure 7.....	15
Figure S1.....	31

## **LIST OF ABBREVIATIONS**

AIC	Akaike information criterion
DEM	Digital elevation model
ENSO	El Niño-Southern Oscillation
IPCC	Intergovernmental Panel on Climate Change
ISODATA	Iterative self-organizing data analysis technique (from ENVI 5.4)
LWM	Low water mark
MHHW	Mean higher high water (tidal datum)
PacIOOS	Pacific Islands Ocean Observing System
SLR	Sea level rise
SOMs	Self-Organizing Maps
sUAS	Small unoccupied aerial systems

## 1. INTRODUCTION

Reef-fronted beaches are important assets providing ecological services (Barbier et al., 2011), storm buffers (El Mrini et al., 2012), critical habitat for coastal flora and fauna, economic development (Houston, 2008), and recreational opportunities for residents and visitors. As beach systems face anthropogenic stressors such as encroaching development and sea level rise (SLR), it is critical that managers have a detailed understanding of environmental processes driving beach change. Yet, carbonate beaches are complex systems that remain poorly understood (Jeanson et al., 2013; Risandi et al., 2020; Segura et al., 2018). Intricate reef bathymetry causes cryptic interactions among natural and anthropogenic forces that make it difficult to isolate cause and effect relationships. Nonetheless, to underpin effective management in a future characterized by SLR (Oppenheimer et al., 2019) and amplified storm impacts (Knutson et al., 2020) it is critical to continue improving our understanding of how and why beaches change.

Royal Hawaiian Beach in Waikīkī (Fig. 1) plays an essential role in Hawai‘i’s tourism-based economy that is valued at ~\$2.2 billion annually (Tarui et al., 2018). Previous studies have established that the beach is characterized by chronic erosion punctuated by seasonal variation (Miller and Fletcher, 2003), and that seasonal morphologic change (Habel et al., 2016) corresponds to summer accretion promoted by south swell, and erosion promoted by local trade-wind swell (intermittent year-round). However, past studies have relied on relatively coarse temporal (quarterly to interannual) and spatial (multimeter) resolution. Considering the critical economic role of Royal Hawaiian Beach, and the rapid growth of anthropogenic stressors (IPCC, 2021), optimized beach management policies need high temporal and spatial resolution monitoring and analysis. Here, we examine multiple physical drivers of beach change using weekly observations from small Unoccupied Aerial Systems (sUAS) to investigate key morphodynamic relationships.

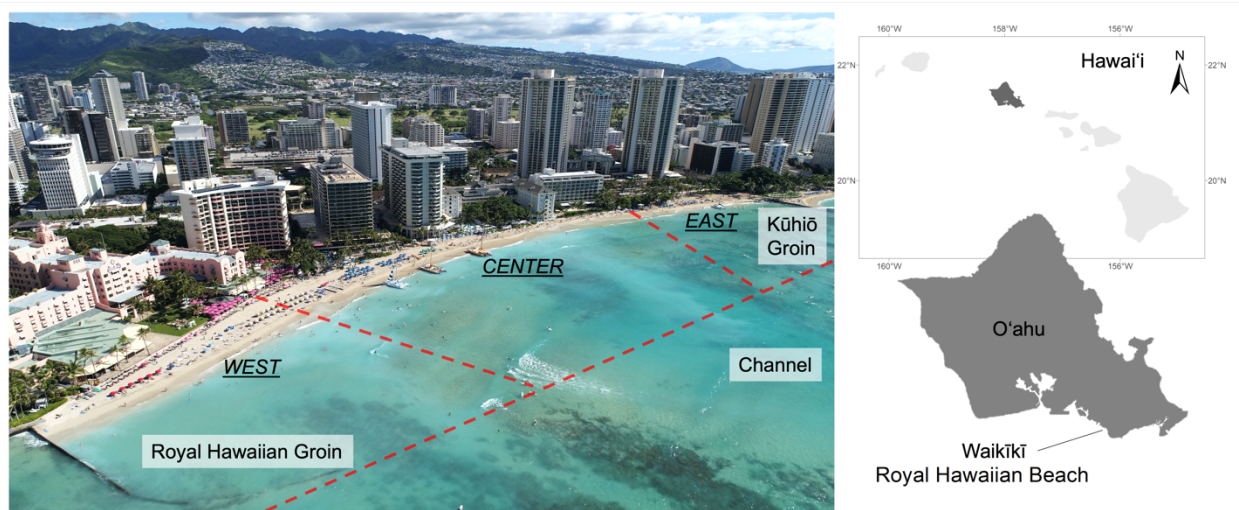


Figure 1. Royal Hawaiian Beach, located in Waikīkī on the south shore of O'ahu, extends 500 m between Kūhiō Groin to the east and Royal Hawaiian Groin to the west. These terminal groins create a littoral cell that is largely closed to external alongshore sand exchange. Also shown are three beach segments used in our analysis (east, center, west; note, the oblique view skews the relative sizes of each section), and less visible, three offshore sand fields. A shallow fringing reef platform influences wave characteristics incident to the east and west portions of the beach (dark benthic substrate). Adjacent to the central portion of the beach a break in the fringing reef forms a shallow, low-relief, sand-filled channel.

The Hawaiian coastline is dominated by variable oceanographic conditions, principally seasonal swell and locally-generated waves. The wave field comprises four dominant regimes (Fletcher et al., 2008; Vitousek and Fletcher, 2008). 1) Winter swells with periods of 14-20 s and breaking face heights of 2-15 m are generated by storms in the North Pacific. These north swells are blocked by the island and have little influence on Waikīkī beaches. 2) Summer swells generated by storms in the Southern Ocean with periods of 14-22 s and heights of 1-5 m are prominent from April to October. 3) Locally-generated trade-wind waves, the most common wave type in Hawai'i, are short period (6-10 s) relatively low height (1-3 m) waves that persist year-round but are most frequent in the summer. 4) Originating from the south or south-west generally in the winter, Kona waves have relatively short periods of 8-10 s with heights of 3-5 m (Homer, 1964). Tropical cyclone swells occasionally impact Hawai'i's shores from June to November bringing greater wave energy that enhances run-up and can drive significant change.

Ocean water level variability is driven by seasonal heating, tidal effects, and interannual patterns (Devlin et al., 2017; Potemra and Lukas, 1999; Widlansky et al., 2020). Monthly

average water levels vary by 0.1 m (typically lowest in March and highest in September). The maximum spring tide range is about 1 m, with highest water levels occurring during the summer spring perigee. Other drivers of water level variability (10's of cm) include mesoscale eddies (Firing and Merrifield, 2004), and interannual thermal and wind field influences (Long et al., 2020). The Honolulu tide station (NOAA, 2020), records a long term SLR of  $1.55 \pm 0.21$  mm/year (1905-2020) that, since the year 2000, has increased to  $3.5 \pm 0.12$  mm/year (data accessed July 2020; Caldwell et al., 2015)

To date, the primary management response to erosion on Royal Hawaiian Beach has been periodic sand nourishment (Wiegel, 2008; Habel et al., 2016) utilizing adjacent shallow reef top sand fields as borrow sites. Typical of other Hawaiian coastal segments (Bochicchio et al., 2009; Conger et al., 2009), nearshore sands in Waikīkī consist of carbonate skeletal fragments produced by the fringing reef ecosystem (Harney and Fletcher, 2003). Most of these sand deposits are thin and redistribute quickly in response to wave energy, consequently covering or uncovering rocky (fossil reef) benthic substrate. These shifts marginally alter bathymetry and roughness, further complicating interactions between waves and nearshore bathymetry. Clear water and shallow conditions permit these shifts in sand cover to be captured in sUAS imagery. Specifically, a sand field with intermittent rocky substrate extends seaward from the toe of Royal Hawaiian Beach several tens of meters and shows changes in sand-rock distribution that vary with beach morphology.

Using two years of weekly sUAS observations, we monitor changes in beach characteristics and compare this history with local wave, wind, and water level records using multiple linear regressions. Of several morphological characteristics, beach volume and width show the strongest correlation to physical environmental variables. Further insights to beach change are revealed using an artificial neural network method known as Self-Organizing Maps (SOMs), which can be used to illustrate topographic variability through time. Our results indicate that interannual variations in width and volume are characterized by alongshore sediment exchange and dominate over seasonal patterns, that show distinct topographic structures.

### **3. METHODS**

Following, we describe our methodology for field data collection, nearshore sand cover delineation, cluster analysis using SOMs, and multiple (and single) linear regressions to correlate

physical variables with field data. Our data collection and processing generally follow a methodology developed by the United States Geological Society (USGS, 2017a, 2017b) in which imagery taken by sUAS is combined with surveyed control points in an iterative process to reduce errors and produce map-quality 3-dimensional surface reconstructions.

### 3.1 Field Data

Seventy-two weekly aerial and ground surveys were collected between April 2018 and February 2020, with a nine-week gap from November 2018 to January 2019. Surveys were scheduled randomly with respect to tide and wave conditions. An sUAS (DJI Phantom 4 pro) collected images at 120 m altitude with 80% front and side overlap, including seven ground control points (GCPs) spaced about 100 m alongshore. Additional control points, collected every 5-10 m using a rod-mounted prism and a Leica TS16 Robotic Total Station, defined the position of the low water mark (LWM) at the seaward edge of the foreshore (Norcross et al., 2002; Fletcher et al., 2003). Existing benchmarks provided a spatial reference using the WGS 1984 UTM Zone 4 projection. Elevations were measured with respect to local mean sea level (LMSL; Datums - NOAA Tides and Currents, present epoch: 1983-2001).

Using Agisoft Metashape and LAStools, a dense point cloud and orthomosaic were generated from sUAS images following standardized USGS protocol (USGS, 2017a, b). The low water mark vector was merged with the sUAS point cloud, and a digital elevation model (DEM) was produced using a natural neighbor interpolation (0.5 m cell size in ArcMap 10.7). Using the ArcMap *volume* tool, beach volume was calculated for each survey, with mean higher high water (MHHW: 0.329 m above MSL) serving as the lower elevation bound. As a result, the seaward boundary was delineated as the location where the beach face intersected the MHHW elevation contour, and the landward boundary was delineated by fixed backshore locations consisting of walls, paths, or other man-made structures. Beach width, the distance between a fixed backshore and the LWM (Norcross et al., 2002), was measured during each survey at >100 cross-shore locations spaced 5 m alongshore. Measurements were subsequently averaged for a beach span of interest.

To quantify an uncertainty estimate for volume measurements, an independent survey was conducted, in which measured point elevations (collected with the Leica TS16 Robotic Total Station, n=198) were compared to modelled point elevations extracted from an sUAS-derived

DEM. We calculate the variance, or standard error, between modelled and measured points ( $SE = 0.005\text{ m}$ ) for use as vertical uncertainty, as we find no bias and assume errors are randomly distributed ( $\mu = 0.004\text{ m}$ ;  $\sigma = 0.068\text{ m}$ ). Volume uncertainty is the footprint beach area times the SE. Beach width uncertainty ( $\pm 0.3\text{ m}$  cross-shore) is attributed to LWM measurement error determined by repeat surveys.

### 3.2 Nearshore Sand Cover

With a simple binary classification (sand vs rock) applied to the shallow marine portion of sUAS imagery, we identify weekly changes in nearshore sand cover. Where correlated to beach volume or width, we interpret this as a proxy for sand exchange between the beach and shallow nearshore (Jeanson et al., 2013; Norcross et al., 2002). Imagery processing to identify changes in nearshore sand cover required cropping orthomosaics to a fixed area (Figure 2). Adjacent to the beach center, the cropped boundary is located approximately 30 m offshore of the beach LWM. Because of weekly variations in turbidity, automated binary classification proved unsuccessful. Instead, we apply an unsupervised classification (ISODATA; Iterative Self-Organizing Data Analysis Technique, ENVI 5.4) to group similar pixels into 10 classes (Fig. 2) (Conger et al., 2005; Doukari et al., 2019; Isoun et al., 2003). Due to high variability in light attenuation characteristics resulting from depth, turbidity, wave breaking, glint, and shadowing, a manual re-classification was required to convert ISODATA results to our final binary dataset, yielding an overall accuracy of 88.8% (see Extended Methodology).

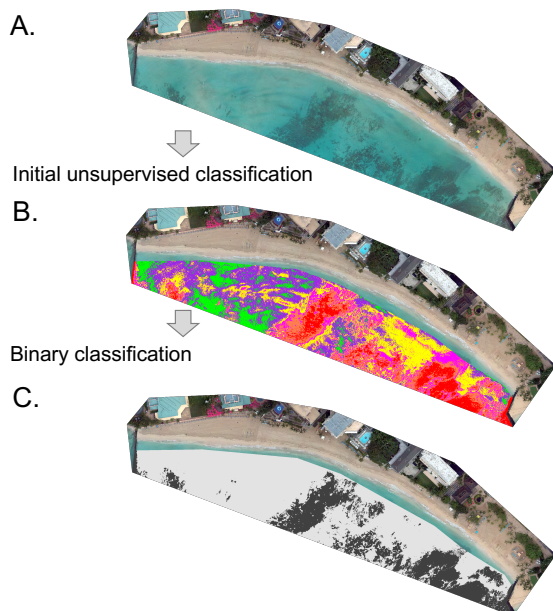


Figure 2. Nearshore sand cover classification. A. unclassified RGB photomosaic; B. Unsupervised classification with ENVI 5.4, ISODATA; C. Manual binary classification. See Extended Methodology.

### **3.3 Self-Organizing Maps (SOMs)**

The week-to-week DEMs produced by our surveys display topographic variability that we examine using Self-Organizing Maps (SOMs). SOMs are visualizations of spatially complex datasets produced by a form of unsupervised machine learning that employs artificial neural networks (Parsons and Coats, 2019). The method reveals the evolution of prevailing patterns under specific conditions and times of year by identifying a mean topography that represents clusters of DEMs with similar elevation patterns (Johnson et al., 2008; Parsons et al., 2018). This is a critical feature of SOMs as other techniques employed in a similar context, such as empirical orthogonal function analysis, may produce spurious spatial structures (Liu et al., 2006; Reusch et al., 2005).

To visualize key topographic features in our 72 DEMs, we employ two SOM analyses. In the first (SOM1), per standard practice (Kohonen, 1990, Johnson et al., 2008), we remove the mean elevation of each grid cell before computing the SOM. For this analysis, we find that seven clusters provides optimal representation of topographic variability—using more than seven clusters resulted in some clusters having only one member, and using fewer than seven clusters failed to capture key variability. In the second analysis (SOM2), in addition to removing the mean elevation of each grid cell, we also remove the mean elevation of the entire beach for each survey. By doing so, this SOM analysis isolates topographic variability independent of changes to beach volume. For SOM2, six clusters were found to best capture the resulting topographic variability, although results were not highly sensitive to this choice.

### **3.4 Physical Variables**

To identify the principal relationships driving changes in beach volume and width, we collect observations of physical variables that represent local environmental conditions (Fig. 3; see also Supplementary Information: Sources of physical environmental variables). We compiled hourly wind direction and speed, ocean water level and tidal range, and calculate wave energy flux generated by local trade winds as well as by swell from the southern hemisphere (see Extended Methodology). Additionally, wave characteristics (significant wave height, peak period, and peak direction) produced by an existing SWAN regional wave model (PacIOOS, 2021a) were extracted from a 0.5 x 0.5 km grid location fronting Waikīkī (Booij et al., 1999; Li et al., 2016). We estimate wave run-up with an existing empirical equation calibrated specifically

for Waikīkī (PacIOOS, 2021b). This equation estimates setup and infragravity swash as a linear function of significant wave height, and incident swash as a function of sea level.



Figure 3. Left column, wave characteristics (top to bottom): Significant wave height (m), peak period (s), peak direction (DegN), south swell energy flux (W/m), and trade-wind swell energy flux (W/m). Right column (top to bottom): Daily average sea level (m), daily tide range (max-min of hourly sea level measurements, m), run-up (m) with a flood elevation threshold of 1.1 m shown in red (PacIOOS, 2021b), wind speed (easterly, m/s), wind speed (westerly, m/s). Winds from the west are sparse but, when present, can drive coastal change.

### 3.5 Multiple Linear Regressions

We use a technique of weighted multiple linear regressions to identify principal drivers of beach change (Anderson et al., 2010; Frazer et al., 2009) (Extended Methodology). Because of bathymetric complexity related to the adjacent fringing reef, wave characteristics influencing the

morphology of the beach display strong alongshore variability. In applying multiple linear regressions, we found poor correlation between physical variables and a representation of the beach in its entirety. Consequently, we identify three physical areas of the beach (east, center, west) for correlation. These beach areas are delineated by two criteria: 1) Topographic structure as reflected in the SOM analyses, and 2) Two locations where beach width shows little variation over the study ( $<5$  m vs  $\pm 13$  m elsewhere) (Fig 1). To characterize drivers of change in each area, we calculate beach volume and average beach width in each segment as predictands and apply the method of multiple linear regressions with physical variables as predictors. All combinations of predictands and predictors (126) were evaluated in light of two rules: 1) To eliminate functions with dependent variables. For example, wave energy flux depends on incoming wave height, period, and direction. As a result, wave energy flux was selected as the representative predictor for waves. 2) For each data group (e.g., wind) all related inputs (e.g., easterly wind, westerly wind) were either all included in a regression model, or not (i.e., there is no regression model that uses only easterly winds, without also including westerly winds). The model assumes that all beach variability is represented in the results. The resulting statistically independent relationships were ranked using an Akaike Information Criterion to identify physical variables most responsible for driving changes in beach morphology.

## **4. RESULTS**

### **4.1 Physical variables**

Figure 3 shows environmental conditions during the survey period. Certain physical variables exhibit distinct patterns: 1) Increases in south swell energy flux show a strong correlation to summer months; 2) Trade-wind swell energy flux varies throughout the year; 3) Water levels fluctuate seasonally; and 4) Tidal range, naturally modulated by the lunar cycle, increases around the summer and winter perigees. Other variables display more anomalous behavior, specifically when assessing wave and water level characteristics during the study. Beginning in July 2019, strong and persistent shifts are seen in significant wave height, peak period, and peak direction that are not seen the previous year. Also beginning in July 2019, trade winds weaken, and water level rises 15-20 cm creating an atypical increase that lasts through the end of the calendar year.

## **4.2 Beach observations**

Figure 4 shows observations of beach volume and width on a normalized scale (0-1) for the entire length of Royal Hawaiian Beach (“total”), as well as for the east, center, and west segments. Each is discussed separately below.

### **4.2.1 Total beach**

Over the first 12 months of the monitoring period, total beach volume increased until approximately April 2019 when it entered a 10-month period of loss for a net decrease of  $-690 \pm 51 \text{ m}^3$ . Superimposed on these long timescale trends, individual loss and recovery events characterize higher frequency variability in beach volume. Three erosional events (2018) in particular show correlation with peaks in trade-wind swell energy. Average beach width remains relatively stable over the first year, but in July 2019 a roughly five-month period of shoreline retreat is observed. The lowest water levels of the survey are seen in February 2019, immediately preceding maxima in total beach volume and width, which are themselves separated by one month. For the entire 22-month period, covariance between total beach width and volume has an  $R^2$  of 0.49 (p-value  $< 0.001$ ), which is lower than the covariance values for the individual beach segments (see below).

### **4.2.2 East beach**

Sand volume over the monitoring period showed no net trend in the eastern segment. However, between October 2018 and July 2019, volume increased as much as 26 percent and then returned to original values by the end of observations. Beach volume and width in the eastern segment showed relatively strong covariance ( $R^2 = 0.73$ , p-value  $< 0.001$ ), with variations in volume typically preceding variations in width. A number of individual events are observed, for example a 7 m increase in beach width followed a strong southwesterly wave event (Kona storm) in February 2019.

### **4.2.3 Center beach**

Sand volume in the center segment closely tracks the beach as a whole, showing 12 months of accretion followed by 10 months of loss. However, no net decrease is observed. Individual volume loss and recovery events create larger relative changes compared to those for the total beach. Short-lived beach width loss and recovery events characterize the entire survey period, although during the first 12 months there was little net change. The correlation between

width and volume is low ( $R^2 = 0.50$  p-value  $< 0.001$ ), and variations in width are generally asynchronous with volume.

#### 4.2.4 West beach

Over the first seven months of monitoring, sand volume in the western segment showed a net increase of 21 percent through November 2018. When observations resumed nine weeks later, this increase had been lost, but returned again by April 2019 and remained relatively constant through the following summer and fall. By November 2019, sand volume dramatically decreased by 35 percent and remained unchanged until February 2020 when observations ended. Overall, beach volume decreased by 20 percent during the course of the study, with beach width following a nearly identical history as quantified by the high covariance value ( $R^2 = 0.65$ , p-value  $< 0.001$ ).

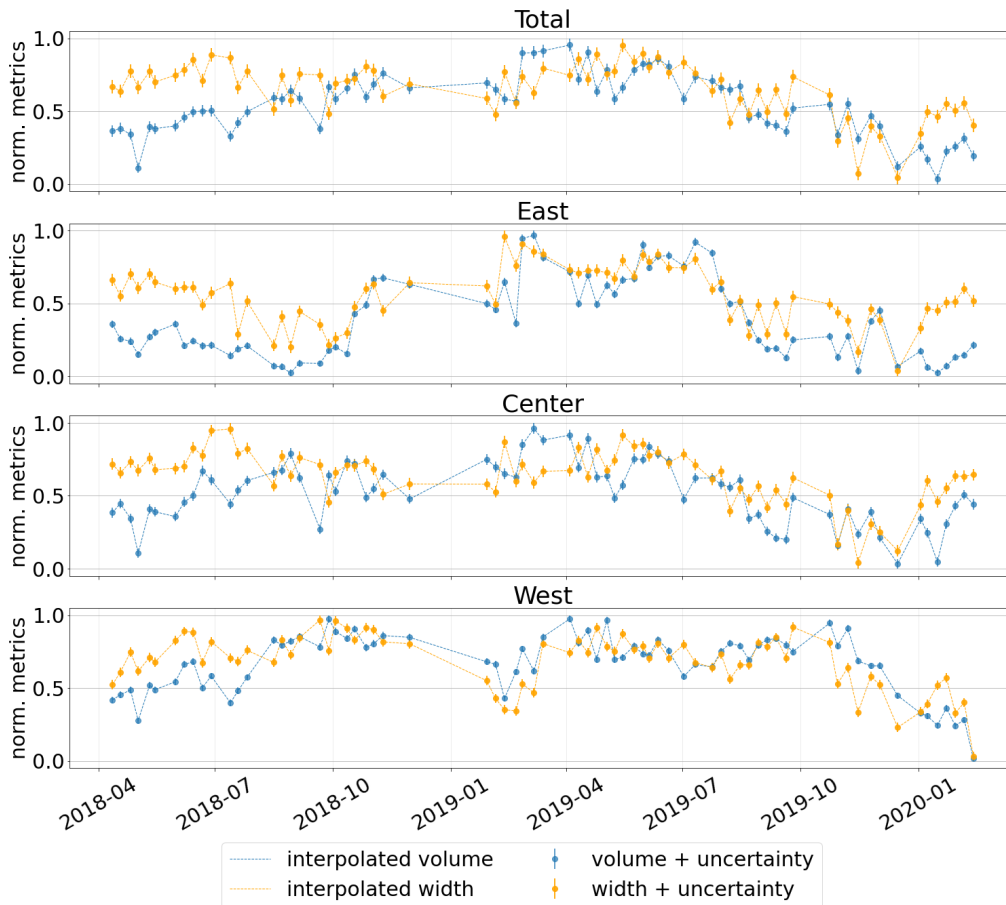


Figure 4. Normalized (0-1) beach observation (circles + uncertainty) and linear interpolation (dashed line) for volume (blue) and width (orange) for the total beach, and segments east, center and west over the two-year survey period. Normalization was achieved from a standard normalizing equation  $(x - x_{min}) / (x_{max} - x_{min})$ .

### 4.3 Nearshore sand cover

In order to improve our understanding of how changes in nearshore sand cover correlate to changes in the adjacent beach, we identify three segments of the sand field that correspond to the east, center, and west beach segments. Variability in percent nearshore sand cover, by segment, is shown in Figure 5. During the 22 months of observation, percent sand cover displayed both high frequency variability as well as longer timescale trends.

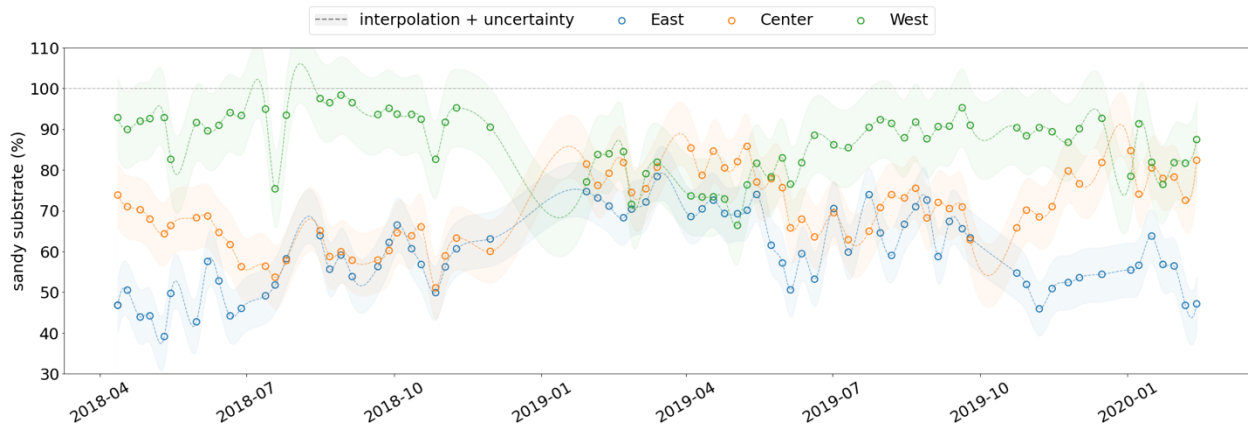


Figure 5. Nearshore percent sand cover adjacent to east, center, and west beach segments. Circles, representing individual surveys, are interpolated by tensioned spline (dashed line). Shading represents quantified error (11.2 percent, Extended Methodology). Note: spline interpolation may exceed 100 percent.

The east sand field, which is generally shallowest and contains the greatest amount of rocky substrate, displayed two distinct long-timescale trends with superimposed high frequency (weekly) fluctuations. A general phase of sand cover expansion (from 40 to 60 percent new sand cover) marked the first 11 months of the study. Beginning in March 2019 and extending to the end of the survey, percent sand cover decreased, ultimately yielding no net change.

The center sand field is characterized by a large rocky outcrop located east of the fringing reef channel. At times, fluctuations in sand cover reduce the surface area of this rocky region as much as 50 percent. Overall, total percent sand cover in the center sand field ranged from 50 to 85 percent. Following an initial decrease in sand cover that ended in August 2018, a slow but persistent expansion peaked in the spring of 2019. Subsequently, percent sand cover showed multi-month trends of expansion and contraction to the end of the survey period.

The west sand field contains the highest proportion of sand in the study area, with only a few areas of rocky substrate. These become buried during periods of high sand cover. Although

highly variable, sand cover generally decreases from 95 percent to a minimum of 70 percent midway through the study, before recovering by the end of the observation period.

The relative pattern of sand cover variability in the east and west sand fields strongly suggest that they exchange sand. Three distinct phases characterize the study period: 1) From April 2018 to January 2019 the eastern sand field shows a slow increase in sand cover while the western sand field, although stable in the early months, ultimately loses about 10 percent of its sand cover over the same period; 2) from January to April 2019, both sand fields stabilize at 70-80 percent sand cover; 3) From April 2019 to the end of the study, the eastern sand field loses 20-30 percent of its sand cover returning to original values, while the western sand field regains the 10 percent sand cover it had lost in phase 1.

We infer from this history, that the western sand field lost sand to the eastern sand field by alongshore transport over the spring, summer, and fall of 2018. This is followed by a period of relative stability extending over the winter and spring of 2019, which ended with alongshore movement of sand returning to the western sand field over the summer and fall of 2019.

#### **4.4 Self-Organizing Maps (SOMs)**

As described earlier, SOMs are a form of neural network cluster analysis that identifies groups of individual DEMs (single surveys) that share similar topographic patterns. Sequential numbering of these clusters indicates order of similarity. That is, clusters with closer proximity in numbering are more similar, and those that are further apart in numbering are more dissimilar. Below we describe the dominant topographic patterns revealed by both SOM analyses (Section 2.3).

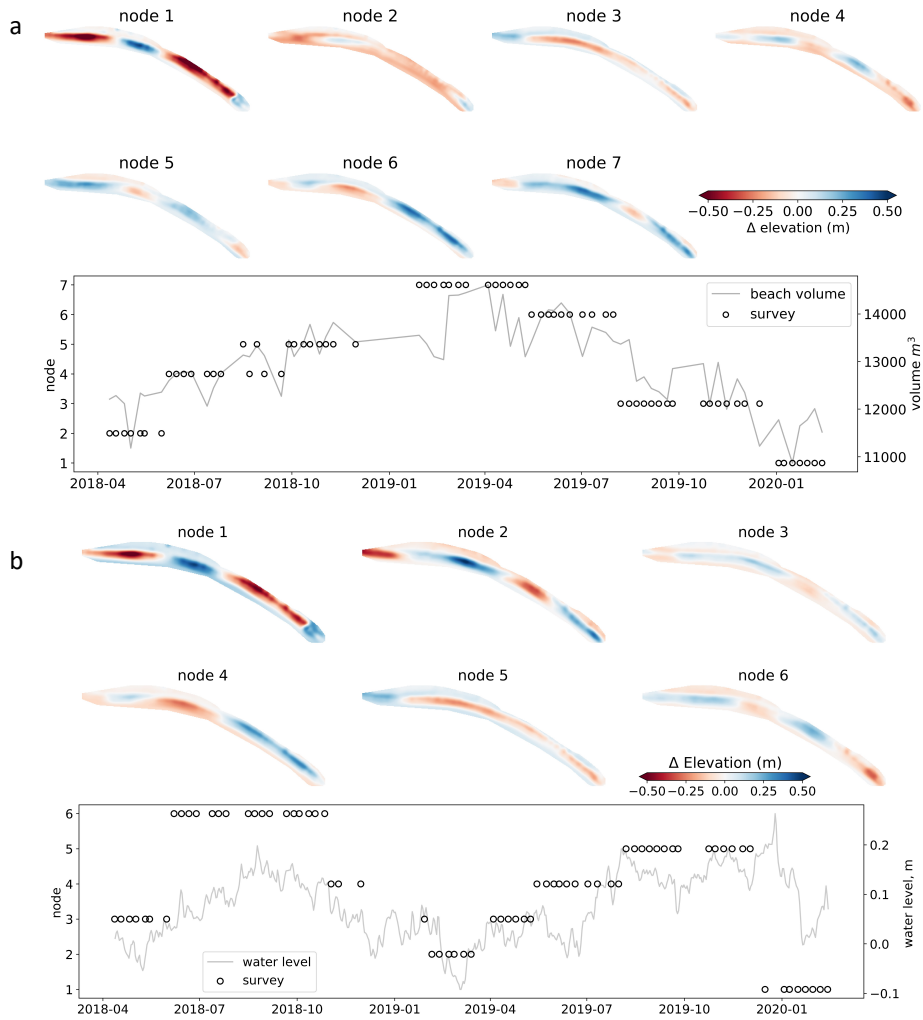


Figure 6. Results from two analyses using SOMs. For each analysis (a and b) DEMs illustrate the mean topography of each cluster. Plots accompanying a and b show individual surveys (open circles) assigned to each cluster (left axis) in chronological order (horizontal axis). a) SOM1 individual survey and cluster chronology resemble beach volume changes (right axis, m<sup>3</sup>). b) SOM2, individual and cluster chronology reveal a seasonal pattern.

#### 4.4.1 SOM1

Figure 6a displays seven DEMs each representing a cluster that captures a particular topographic structure. Additionally, beach volume (right axis) variability is graphed along with the cluster assignment of each of the 72 surveys (open circles, left axis). The graph shows a strong correlation between beach volume and cluster assignment. Over the entire study period, the correlation shows that higher numbered clusters correspond to periods of high beach volume, and lower numbered clusters to low beach volume. Clusters 1 and 7 correspond to volume minima and maxima (resp.) and share an area of higher elevation in the center. During volume

minima (cluster 1) elevation is low to the east and west, suggesting these are areas of erosion. Clusters 4 and 5 correspond to phases of increasing volume (esp. to the east and west), over the course of 2018. Clusters 6 and 3 describe the period July to December 2019 when beach volume and width decreased. In temporal order, cluster 6 shows widespread sediment loss in the transition to cluster 3, suggesting that erosion originates in the central region.

#### **4.4.2 SOM2**

The graph in figure 6b illustrates a strong seasonal influence as shown by clusters 1-3 (winter and spring) and clusters 4-6 (summer and fall). Clusters 4 and 3 operate as transitional topographic signatures between summer and winter end states. This implies that variations in beach topography retain a seasonal structure although changes in beach volume (see Figure 6a) do not.

Summer season at Royal Hawaiian Beach is characterized by large swell arriving from the southern hemisphere. Cluster 6 dominates the summer of 2018, and cluster 4 dominates the summer of 2019. Both clusters show low topography in the area of the central beach segment, and higher topography to the east and west.

Water level shows seasonal characteristics with some correspondence to topographic signatures (SOM2). However, passive water level alone is not an effective driver of beach change. Waves or some other energetic environmental process is needed to reshape a beach profile. Clusters 5 and 6, which have close similarity indicated by their numeric order, develop during the summer and fall of 2018 and 2019 at times of high water-level and strong south swell.

#### **4.5 Regression Analysis**

As described in Methods (Section 2.4), a system of weighted average multiple linear regressions (Anderson et al., 2010) was used to establish the strength of correlation-based relationships between physical environmental parameters that are likely to drive beach change (swell, wind, water level) and indicators of beach response (volume, width). Model predictions are shown in Figure 7 along with observed volume and width.

Additional single linear regression models were used to: 1) identify correlations between beach indicators (volume and width) and development of the three sand fields located

immediately offshore, and 2) investigate correlations between single physical drivers and beach response.

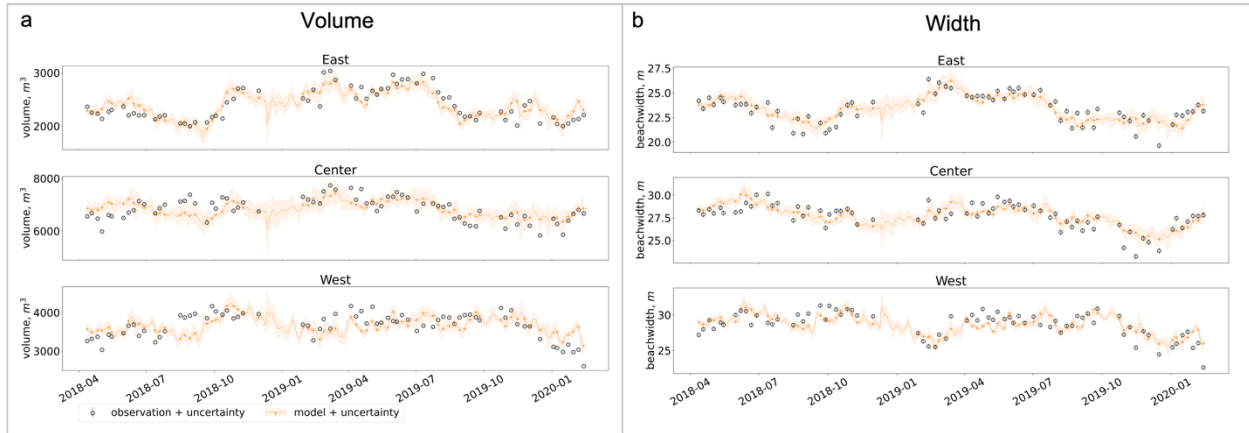


Figure 7. Multiple linear regressions model (orange line + uncertainty) for beach volume (a) and beach width (b) at east (first row), center (second row), and west (third row) beach segments. Survey data (black circles + uncertainty); model data for survey dates (orange '+').

Table 1 presents two approaches to correlating environmental variables (left column) with variations in beach volume and width. The section labelled “1:1 Correlation coefficient, Single regression” lists Pearson Correlation Coefficients describing single linear regressions between environmental variables and beach characteristics. The section labelled “Proportion explained (%), Multiple regression” shows results of the multiple linear regressions model (results also shown in Figure 7).

Variable	Group	n days	Single regression: 1:1 Correlation coefficient						Multiple regression Proportion explained (%)							
			Volume			Width			Volume				Width			
			east	center	west	east	center	west	east	center	west	total	east	center	west	total
Energy flux south	swell	Filter*	0.15	0.15	<b>0.32</b>	0.03	<b>0.36</b>	<b>0.59</b>	12.7	15.6	<b>36.1</b>	21.5	6.6	17.3	<b>32.7</b>	18.9
Energy flux trades	swell	Filter*	<b>-0.29</b>	<b>-0.31</b>	0.10	<b>-0.24</b>	<b>-0.26</b>	0.09	11.4	17.8	14.2	14.5	10.2	5.1	12.8	9.4
Wind speed West	wind	50	<b>0.57</b>	<b>0.37</b>	0.07	<b>0.56</b>	0.12	-0.19	4.2	5.0	10.2	6.5	5.2	14.8	13.7	11.2
Wind speed East	wind	50	<b>-0.66</b>	<b>-0.30</b>	-0.12	<b>-0.43</b>	0.17	<b>0.30</b>	<b>38.9</b>	15.0	10.7	21.5	15.1	24.9	22.3	20.8
Water Level	water	30	<b>-0.56</b>	<b>-0.50</b>	0.09	<b>-0.78</b>	<b>-0.58</b>	-0.08	24.1	33.4	11.1	22.9	<b>52.8</b>	<b>31.1</b>	7.4	30.4
Tidal range	water	7	-0.13	-0.13	<b>-0.24</b>	-0.16	-0.13	<b>-0.24</b>	8.3	12.8	17.6	12.9	10.1	6.7	11.1	9.3
Run-up	water	7	-0.10	<b>-0.26</b>	0.03	<b>-0.23</b>	-0.07	<b>0.30</b>	0.4	0.5	0.2	0.4	0.0	0.0	0.0	0.0
Total									100.0	100.0	100.0	100.0	100.0	100.0	100.0	100.0

Table 1. Results showing environmental parameters (column 1, far left), group name (column 2), and parameter time series averaging window (column 3). Columns 4-9 show correlation coefficients for individual pairings of environmental parameters and beach indicators (single linear regressions); beach volume (columns 4-6), beach width (columns 7-9). Bold indicates significant relationships (p-value < 0.05). Columns 10-17 show results of the

multiple linear regressions model (see Extended Methodology for description), indicating the proportion (%) of change explained by each variable for the three beach segments (east, center, west), as well as for the total beach; beach volume (columns 10-13), beach width (columns 14-17). Blue indicates an increase in beach volume or width resulting from an increase in an environmental variable; Red indicates a decrease in beach volume or width resulting from an increase in an environmental variable. Filter\*: A weighted average filter, in which weights decay exponentially over time, applied to wave energy. We use a 27-day recovery parameter (Dail et al., 2000; See Extended Methodology)

#### **4.5.1 Beach volume**

Using multiple linear regressions, we find that changes in beach volume are nearly equally responsive to water level variations (36.1 percent), wind conditions (28.0 percent), and wave energy flux (35.9 percent). These are discussed individually below.

Variations in water level show the strongest influence on seasonal beach volume variability. Low water levels in winter months generally correspond to beach volume increases while high summer water levels correspond to beach volume losses. Water levels appear to modulate longshore sediment transport; high water levels (allowing increased wave energy to cross the fringing reef) correlates to volume loss from the east and center beach segments, and volume gains in the western beach segment. Tidal range varies bimonthly with the lunar cycle and there is a general correspondence of beach volume loss to tidal range increases.

Wind characteristics explain approximately one fourth of the observed variability in beach volume, but the relationship is complex. Strong winds from the east (hereafter “trade winds”) correspond to beach volume losses, with larger erosion in east and smaller erosion in west. Westerly winds correspond to increases in beach volume at the center and west beach segments, but the effect on the east beach segment is ambiguous (~5% variance explained). However, single linear regressions indicate that east beach volume may increase during westerly winds.

We find that wave energy flux shows strong correlation to changes in beach volume. Increases in south swell energy flux correspond to beach volume gains at all beach segments and is the dominant control for the west beach segment. The east and center beach segments show pronounced erosion, and the west beach segment pronounced accretion, as a result of increases in trade-wind swell energy flux.

Using single linear regressions to improve understanding of sediment dynamics, we find correlations between beach volume and the nearshore sand cover (results not shown). However, these correlations are not strong for adjoining pairs of subaerial and nearshore beach segments. Instead, the relationships between nearshore sand fields and non-abutting subaerial beach segments show varying correlations. The east sand field is positively correlated with beach volume at all three beach segments. This indicates that increases in the east sand field are contemporaneous with increased beach volume at all three beach segments. The west sand field is inversely correlated with beach volume at the east and center beach segments, suggesting that sediment exchange occur between the west sand field and the center/east beach segments. These correlations reveal that sand exchange with the shallow sea floor in front of Royal Hawaiian Beach is a critical aspect of littoral processes

#### **4.5.2 Beach width**

Using multiple linear regressions, we find that changes in beach width are driven by water level variations (39.7 percent), wind conditions (32.0 percent), and wave energy flux produced by south and trade-wind swell (28.3 percent). Overall, the multiple linear regression model finds stronger correlations to changes in beach width than to changes in beach volume. Additionally, it does a good job of representing smaller and shorter timescale (weekly) responses in beach width that correspond to the tidal cycle and to peaks in wave energy flux.

Water level variations are important in regulating beach width. Notably the influence of water level variations is seven times higher for the east segment (52.8 percent) compared to the west segment (7.4 percent). High water levels, and tidal range, correspond to beach narrowing at all beach segments. Like changes in beach volume, water level variations exert strong seasonal variability in beach width.

South and trade-wind swell energy explain 28.3 percent of beach width variations. The west segment is most responsive to swell energy. A seasonal signal is recorded in the south swell energy flux, with increases during summer months corresponding to beach widening at all segments. Trade-wind swell energy, on the other hand, corresponds to beach widening at the west beach segment and narrowing in the center and east beach segments.

Variations in wind drive changes in beach width, although this influence is strongest in the central and west beach segments. During times of strong trade winds, the west and center

beach segments widen while the east beach segment narrows. Winds from the west drive widening across the entire beach, and most strongly at the center.

Strong correlations also exist between beach width and variations in the nearshore sand field. Using single linear regressions, we find that the center sand field inversely correlates to changes in width at the center and west beach segments. This suggests that sediment increases in the center sand field correspond to sediment losses at the west and center beach segments, further strengthening our understanding of nearshore sediment dynamics. Amongst the nearshore sand fields, we find that the east and center sand fields change in unison, but are negatively correlated to variations in the west sand field.

#### 4. DISCUSSION

Weekly sUAS monitoring coupled with traditional ground surveys of key beach features provides a unique high-resolution dataset to improve understanding of fundamental coastal processes governing the stability of Royal Hawaiian Beach. Specifically, using multiple (and single) linear regressions, SOMs, remote sensing, and existing nearshore wave and runup models, we identify key relationships driving changes in beach volume and width. Together, these analyses allow for the linking of sediment sources and sinks, under specific wave, wind, and water level conditions, as discussed below (and summarized in Table 2).

Drivers		Responders	
		Sand receivers (+)	Sand sources (-)
1	Low wind trade conditions	West beach & sand field	East beach & sand field Center beach & sand field
2	High wind trade conditions	West sand field	East beach & sand field Center sand field
3	South swell energy flux	East beach Center beach West beach & sand field	East sand field Center sand field
4	Kona storms	East beach & sand field	West beach
5	Quiet conditions	East beach Center beach West beach	-
6	Westerly winds	East sand field Center beach & sand field West beach	West sand field
7	High water levels & South swell	West beach & sand field	East beach & sand field Center beach & sand field
8	High water levels & other waves	West sand field	East beach & sand field Center beach & sand field West beach

Table 2 Important physical processes that drive beach change, and related responses in beach and nearshore sand bodies.

#### **4.1 Trade conditions**

Trade conditions, including trade-wind swell energy flux and easterly trade winds, generally drive alongshore sediment transport from east to west. We differentiate between two trade conditions 1) low wind speed trades and 2) high wind speed trades. Conditions during low wind speeds exhibit the strongest alongshore sediment exchange. The west beach segment widens while the east and center beach segments narrow. The sand fields mirror this pattern; the west sand field gains sand whereas the east and center sand fields lose sand.

Compared to low winds, high wind speeds drive accelerated erosion on the east beach segment and sand field, whereas the west beach segment and sand field show reduced accretion. The center segment responds by widening but also losing volume. Overall, this response to high wind speed trades may reflect the influence of wave driven circulation and setup in the center region. That is, offshore flow may interrupt the alongshore delivery of sediment from the east to the west by pushing sand out into the channel, that had accreted on the center beach segment.

#### **4.2 South swell energy flux**

Strong south swell corresponds with increases in volume and width in all beach segments. Decreases in the east and center sand fields suggest that these function as sediment sources for the entire beach. However, the west sand field increases during south swell, possibly due to sediment buildup against the western groin. The nearshore sand channel, located in the center region, could function as a sediment source where south swell mobilizes and delivers sand from offshore sources. These findings generally agree with the consensus that south swell energy flux drives beach accretion at Royal Hawaiian Beach (Habel et al., 2016; Miller and Fletcher, 2003).

#### **4.3 Kona storms**

From raw observations we find that southwesterly Kona storms reverse the direction of alongshore currents and drive sediment from west to east (Miller and Fletcher, 2003). Following a strong westerly Kona storm in February (2019), we observed a 7 m increase in beach width on the east beach segment. At the west beach segment, a ~1 m high erosional scarp formed. We suspect sediment was transported alongshore from west to east, where it built up against the Kūhiō groin and adjacent shallow reef (< 0.5m deep).

#### **4.4 Quiet conditions**

During quiet conditions, we observed general accretion at all beach segments, and little change in the nearshore sand fields. The period between January and May 2019 is characterized by low wave activity, relatively low water levels and consequently small run-up. Trade winds became less persistent while westerly winds became more frequent compared to the same period in the previous year. During this relatively quiet period, beach volume and width maxima were reached by April and May, respectively, suggesting that quiet conditions (e.g., low energy) are favorable to overall beach accretion.

#### **4.5 Westerly Winds**

Westerly winds are the dominant factor controlling variations in the nearshore sand fields. Strong westerly winds, as well as Kona storms, drive alongshore sediment transport from west to east; the west sand field loses sand, and the center and east sand fields gain sand. The west sand field is thus the likely sediment source for increases in the west and center sand fields and beach segments. Westerly winds are also correlated to changes in the east beach segment that include increased width (4.2 percent) and decreased volume (-4.2 percent).

#### **4.6 High water levels**

High water levels enhance alongshore sediment transport (Grady et al., 2013), and generally erode the east and center beach segments yet build the west beach segment. However, these relationships are complex. In general, it is useful to differentiate between 1) elevated water levels during increased south swell energy flux, and 2) elevated water levels during other types of wave activity. During all types of wave activity, the east and center beach segments lose sand, and the west sand field gains sand. During elevated water levels that are coincident with increased south swell energy flux, the west beach segment receives sand from the center and east beach segments. However, elevated water levels coupled with short period waves tend to erode the west beach segment (e.g., October 2019) without clear increases occurring in offshore locations. Persistent elevated water levels, as seen from September 2019 through the end of the calendar year, were associated with beach narrowing at all segments.

#### **4.7 Differences between segments**

Although it is clear that the individual beach segments and nearshore sand fields readily engage in sand sharing, alongshore variations in bathymetry and orientation create unique conditions under which the individual beach segments respond differently to physical processes. For instance, the east beach segment has the shallowest offshore region (Habel et al., 2016) of the three and is influenced most strongly by water level variations and tidal range. Because depth changes across the fringing reef strongly amplify or suppress the impact of wave conditions, small differences in water level may have a significant influence on beach processes. This is reflected in the regression analyses where, as compared to the west segment, water level in the east carries seven times more influence in driving changes in beach width and two times more in driving changes in beach volume.

Of all environmental parameters, wave energy exerts the greatest influence on driving changes in the west beach segment, with higher wave energy generally corresponding to width and volume gains. The western nearshore region has the lowest proportion of fossil reef patches, resulting in greater wave energy reaching the shore. Further, wave energy may suspend sediments, which are then transported in the dominant current direction (westerly), where they accrete against the western groin. The center beach does not respond to one exclusive driver. Variations in width correlate strongest to wind conditions, whereas wave energy exerts the largest changes in volume.

Under several conditions, the east and west segments have opposite responses. For example, during high water levels the west segment gains sand at the expense of the east segment. The same pattern is true for increases in trade conditions, suggesting these are mechanisms that enhance alongshore sediment exchange.

#### **4.8 Profile response**

A standard model of beach morphology response to forcing describes a cross-shore reduction in slope associated with high energy, wave driven profile erosion (Wright and Short, 1984). A dissipative morphology consists of an offshore sandbar composed of sand eroded from the foreshore region that shallows the seafloor sufficiently to cause wave energy dissipation. As wave energy wanes, the sandbar migrates landward creating a series of shallow surf zone

features and eventually accretes onto the foreshore. This steepens the profile marking a reflective morphology.

We sought to project this standard model onto the results of our analysis and found that the fundamental characteristic of onshore loss (gain) balanced by offshore gain (loss), that we will refer to as profile asymmetry, was absent. Instead, we observed profile symmetry consisting of onshore and offshore portions of the profile gaining and losing sand at the same time. However, we discovered asymmetry in the longshore component of our observations. For example, trade conditions drive sediment loss from the eastern region (including both the beach segment and the nearshore sand field) and sediment gain in the western region of Royal Hawaiian Beach. Similarly, Kona winds drive sediment loss in the west and gain in the east.

Norcross et al., (2003) examined a cross section of representative beach systems in Hawai‘i and found in all cases that longshore transport dominated seasonal beach development despite the study sites being located in different meteorologic and oceanographic settings. From this, we conclude that although aspects of the standard model such as profile steepening and short-term cross-shore sediment transport are found on Hawaiian beaches (Habel et al., 2016), researchers should not assume that profile asymmetry controls beach morphology.

#### **4.9 Implications for management in a changing climate**

We find that trade conditions and water level variability play large roles in modulating wave energy across the fringing reef surface. These processes work in conjunction with other physical parameters to drive sediment exchange and therefore constitute fundamental conditions governing beach stability. As such, factors influencing short-term and long-term water level variations, as well as trade conditions, should be closely considered by beach managers. These may include, for example, extreme tides (king tides), the El Niño-Southern Oscillation (ENSO), and long-term sea level rise.

High-tide flooding is present in Honolulu during summer perigee king tides and can result in wave overwash of the coastline, beach erosion, and disruptions to local economic activity (Banno and Kuriyama, 2020; Hino et al., 2019). The frequency of high-tide flooding is found to precipitously increase around the mid-2030s as a result of long-term sea level rise and nodal cycle modulations of tidal amplitude (Thompson et al., 2021). The number of days where high tide exceeds 35 cm above MHHW plateaus at 40-45 days/year until the year 2035. A

dramatic increase is predicted to 152 days/year by 2040, and 254 days/year by 2045 for RPC8.5 (Thompson et al., 2019). These increases of high-tide flooding events mean more short-term high frequency episodes of deepening across the fringing reef, thus allowing increased wave energy flux impacts and associated sediment movement.

Wind and water level conditions in Hawai'i are modulated by ENSO. Increases in extreme El Niño events are projected for the coming decades (Cai et al., 2014), although there is uncertainty in these projections (Stevenson et al., 2021). If these projections are correct, local El Niño impacts like low trade conditions, increased swell energy, and elevated sea surface temperature should become more common. Strong El Niño events are also associated with a delayed (1-2 years) increase in ocean water level as water level anomalies propagate westward as a Rossby wave, as observed following the 2015 El Niño (Long et al., 2020). By contrast, La Niña events are associated with strong trade conditions. The frequency of extreme La Niña events has also been projected to increase, doubling in frequency by 2100 (Cai et al., 2015). La Niña events, in triggering strong trade conditions, can be expected to generate beach erosion and loss. But, the resulting increase in alongshore sediment transport may generate accretion to the west depending on underlying environmental conditions.

As stated earlier, the Honolulu tide gauge shows a recent increase in the rate of SLR. This is consistent with projections of accelerating global mean sea level rise (IPCC, 2021). Although SLR has inherently long timescales, it amplifies the impacts of higher frequency events like king tides and ENSO-related water level variability. Critically, SLR may not be mitigated by reef accretion because of the negative influence of ocean acidification and high sea surface temperature (Hoegh-Guldberg et al., 2007; Pandolfi et al., 2011). Radiocarbon dating of reef structures in Hawai'i identifies the fringing reef as a fossil structure formed approximately 2000 yrs BP (Grossman et al., 2006), further suggesting that because of inimical nearshore conditions, the reef may not accrete under SLR. Managers should thus anticipate that SLR will increase depth over the fringing reef leading to higher wave energy and sediment movement in the beach and nearshore area that can accelerate erosion.

Over the course of the study, we observed that elevated water levels likely reduced beach recovery following high energy events. For example, during fall 2018, three episodes of trade-wind swell resulted in significant beach loss, which was fully recovered within one week. However, during the fall of 2019, coincident with an atypical increase of elevated water level,

the beach did not recover from similar peaks in trade-wind swell energy. This resulted in the observed beach volume falling below the initial survey volume. This period was also characterized by increased nearshore wave activity despite there being no measured increase in swell energy (See Figure 3). This suggests that 1) beach recovery may be hindered by high water levels and 2) seasonal and interannual water level increases may drive amplified beach erosion (Abessolo et al., 2020; Segura et al., 2018; Theuerkauf et al., 2014). If true, and given that water levels will continue to rise, Royal Hawaiian Beach may be less resilient in the future.

## **5. CONCLUSIONS**

Weekly surveys of a reef-fronted beach system coupled with image classification of nearshore sand fields provide insight into unique sand source-sink networks that vary under a range of environmental conditions. Generally, individual beach segments and their adjacent sand field gain and lose sand in unison, which differs from the standard reflective/dissipative beach model. Alongshore transport dominates sediment dynamics and environmental conditions, such as elevated water levels, trade conditions, and Kona storms, enhance this alongshore sediment exchange. The primary environmental drivers of beach change are water level variability and wave energy flux. Bathymetric complexity related to the adjacent fringing reef causes alongshore variability in beach response. Further analysis using SOMs suggests that beach topography retains a seasonal structure, although changes in beach volume reflect interannual variability.

This work improves understanding of sediment dynamics and complex beach responses to environmental variables on a reef-fronted beach. Our results suggest that a future characterized by SLR and amplified ENSO events may accelerate erosion and contribute to destabilizing the Royal Hawaiian Beach, and possibly geologically similar beach systems, and thus managers should expect increased cost of beach maintenance in the future.

## **APPENDIX A: EXTENDED METHODOLOGY**

In the following, we describe a comprehensive methodology for nearshore sand cover delineation, calculation of environmental variables, and use of multiple linear regressions for correlating physical variables and beach response.

### **1. Nearshore Classification**

An unsupervised classification (ISODATA; Iterative Self-Organizing Data Analysis Technique, ENVI 5.4) was used to group similar pixels into 10 classes. Using fewer classes resulted in classes containing both rocky and sandy substrate. Only green (532 nm) and blue (468 nm) bands (Burggraaff et al., 2019) were used for classification as the red band introduced noise due to strong attenuation and resulted in misclassification.

The resulting 10 classes were manually assigned to either 1) rocky substrate, 2) sandy substrate, or 3) unclassified. Unclassified pixels consisted of whitewash or extreme sun glint, and generally comprised a small segment of the mosaic (96 % of surveys, n=69, had less than 2% of pixels unclassified). A single survey had extremely turbid water conditions, resulting in  $\approx$ 15% unclassified pixels.

We assess classification accuracy from five representative mosaics characterized by 1) clear water, 2) turbid water, 3) surf, 4) sunglint, and 5) shadows, respectively. Most images had relatively clear water, so this assessment gives a representative but conservative error estimate. For each mosaic, 50 random points were generated, and benthic substrate (rock vs. sand) at each point was manually annotated. The accuracy was determined from the percentage of correctly classified points, giving 88.8%.

### **2. Environmental Variables**

Wave energy flux generated by southern hemisphere swell and trade-wind waves were calculated from a subset of the wave spectra characteristic of each swell (Fletcher et al., 2008). We define south swell as waves with periods of 13-30 s from a direction of 147-220 DegN, and use wave measurements from a buoy located on the south shore of O‘ahu (PacIOOS Wave Buoy 233). We define trade-wind waves as waves with periods of 3-10 s from a direction of 45-160 DegN and use a buoy on the east shore of O‘ahu (PacIOOS Wave Buoy 098). Wave energy flux (W/m) was calculated by taking the sum of energy density in relevant frequency and directional

bins. Then, we multiply this energy density with peak wave period for each timestep. It should be noted that we do not include constants in these calculations, as we remove the mean for model calculations. So, these values are proportional to the true wave energy flux.

Wind speed and direction was obtained from Honolulu Airport, approximately 10 miles from Waikīkī. Based on direction, winds were separated into trade winds (22.5 – 112.5 DegN; Garza et al., 2012), and westerly winds (200 – 290 DegN). Measured wind speed within each bin was used as wind characteristics.

We compiled ocean water level from datum-controlled hourly tide gauge data from Honolulu Harbor from the University of Hawai‘i Sea Level Center Fast Delivery database (<http://uhslc.soest.hawaii.edu:80/pendap/fast/hourly/h057.nc>, accessed July 2020; Caldwell et al., 2010). We define tidal range as the difference between highest and lowest hourly water level each day. Run-up was calculated with an existing equation developed for Waikīkī (<http://www.pacioos.hawaii.edu/shoreline/runup-Waikīkī/>). This equation estimates setup and infragravity swash (long-period gravity waves) as a linear function of significant wave height ( $H_0$ , From PacIOOS wave buoy 233), and incident swash (short-period gravity waves) as a function of sea level ( $sl$ ) at a vertical datum of mean lower low water (MLLW). The run-up equation is as follows

$$runup = 1.2 \left( su + \frac{S}{2} \right) \quad (E1)$$

$$S = \sqrt{S_{inc}^2 + S_{IG}^2} \quad (E2)$$

Where  $su$  is setup ( $su = 0.0655 \cdot H_0$ ),  $S_{IG}$  is infragravity waves ( $S_{IG} = 0.275 \cdot H_0$ ), and  $S_{inc}$  is incident swash ( $S_{inc} = 0.313 \cdot sl$ )

### 3 Multiple Linear Regression

#### 3.1 Conditioning environmental variables

Environmental variables used to model beach volume and width included south swell, trade-wind swell, westerly winds, trade winds, water level, tidal range, and run-up. These variables were evaluated in two different ways to reflect conditions preceding each survey. Water level, wave run-up, tidal range, and wind characteristics were conditioned with an averaging window. Generally, we determined window size using single linear regressions between each environmental variable and beach characteristic, and picked the averaging window

with the best fit (highest  $R^2$ ) (Segura et al., 2018). However, this varied across beach segments and between volume and width, so we used a window size close to the mean of optimal windows between segments and volume and width.

For wave energy flux, we apply a decay filter such that recent values are weighted higher, therefore resolving peaks in wave energy that otherwise diminish with an averaging filter. The filter is adopted directly from Dail *et al.* (2000), fitted to Waimea bay, O‘ahu, Hawai‘i. It calculates a decay filter for wave energy flux ( $F$ ), with a beach recovery ( $\phi$ ) of 27 days, and an impact time ( $D$ ) of 60 days.

$$Flux = \left( \sum_{i=1}^D 10^{-\frac{d}{\phi}} \right)^{-1} \cdot \sum_{i=1}^D F \cdot 10^{-\frac{d}{\phi}} \quad (E3)$$

### 3.2 Eliminating dependent variables

To ensure no dependent variables are in the same model, we include only wave energy flux from south and trade-wind swell, and not the SWAN simulated nearshore waves. We choose to couple each group, such that variables within a group are either included or excluded. For example, south swell and trade-wind swell are either both included or not included, as we assume that it is the set of conditions that alter the beach rather than just a single component.

### 3.3. Least squares multiple linear regressions

With the conditions mentioned above, 62 unique models were generated. We use ordinary least squares multiple linear regression to fit the 62 combinations of environmental variables to beach response using the following process model:

$$d = Gm + \eta \quad (E4)$$

Where  $d$  is an ( $N \times 1$ ) vector of observations,  $G$  is the system matrix ( $N \times M$ ), in which each column of  $G$  represents an environmental variable,  $m$  is the parameter vector ( $M \times 1$ ) of model coefficients (slope), and  $\eta$  is an ( $N \times 1$ ) vector of noise, from a zero-mean, Gaussian noise process with covariance matrix  $C_d$ . Our noise model accounts for 1) measurement errors, and 2) correlation of model residuals in space and time. Observational and environmental data are conditioned by removing the mean.

### 3.4 Accounting for correlation of model residuals

To test for correlation, we assess model residuals from the most complex model (with seven parameters) initially assuming no correlation. We first define  $C_d$  using explicit measurement uncertainty:

$$\tilde{C}_d = W^{1/2} C_{corr} W^{1/2} \quad (E5)$$

Where  $W$  is a  $(N \times 1)$  vector of squared measurement errors (width: fixed 0.3 m, volume: 0.005 x area), and  $C_{corr}$  is an  $(N \times N)$  identity matrix. The parameter vector,  $\hat{m}$ , and predicted beach volume or width,  $\hat{d}$ , is calculated:

$$\hat{m} = (G^T \tilde{C}_d^{-1} G)^{-1} G^T \tilde{C}_d^{-1} d \quad (E6)$$

$$\hat{d} = G \hat{m} \quad (E7)$$

From these residual ( $\rho = \hat{d} - d$ ) we find autocorrelation through space, but only in adjoining beach segments. We find essentially no autocorrelation through time, even though our input environmental variables are time averaged. Therefore, we adjust  $C_{corr}$  to correct for spatial autocorrelation of adjoining beach segments. If we consider  $C_{corr}$  as a 3x3 block matrix (3 beach segments) of 72x72 entries each (n surveys), the adjustment for 1-lag spatial autocorrelation will occur at the blocks (1,2), (2,1), (3,2), and (2,3). Each block matrix contains nearly identical values along the diagonal because the autocorrelation between east & center and center & west were very similar. The correction for spatial autocorrelation is calculated as a scaled sum of residuals multiplied between sections, defined as  $R$ :

$$R = \left( \sum \rho^2 \right)^{-1} \left( \sum \rho_{east} \rho_{center} + \sum \rho_{center} \rho_{west} \right) \quad (E8)$$

The updated correlation matrix  $C_{corr}$  has ones on the main diagonal,  $R$  along the diagonals of the blocks (1,2), (2,1), (3,2), and (2,3), and zeros elsewhere. After two iterations the values converge, and the final  $C_{corr}$  and  $\tilde{C}_d$  for that model is reached. Then, predicted values are calculated with (4) and (5).

### 3.5 Model averaging

Akaike's Information Criterion (AIC) is used to assess model fit, which is defined as the following:

$$AIC = N \ln(\hat{\alpha}) + \ln|C_{corr}| + (N - df) + 2k \quad (E9)$$

Where  $N$  is the number of observations and  $df$  are degrees of freedom which here are equal to  $k$ ; the number of variables.  $\hat{\alpha}$  is the constant of proportionality and calculated as:

$$\hat{\alpha} = (d - G\hat{m})^T \tilde{C}_d^{-1} (d - G\hat{m}) / (N - df) \quad (E10)$$

Models were very similar with respect to their AIC values. Therefore, we employ a weighted model average based on AIC scores (Frazer et al., 2009). As per standard practice,  $\Delta AIC$  is determined by subtracting the best fit (lowest) AIC value from all scores;  $\Delta AIC = AIC - \min(AIC)$ . Then, model weight  $w_j$  for each model  $j$  is:

$$w_j = \frac{\exp\left(-\frac{1}{2} \Delta AIC_j\right)}{\sum_j \exp\left(-\frac{1}{2} \Delta AIC_j\right)} \quad (E11)$$

The weighted average model ( $\phi$ ) is found by multiplying each model prediction ( $p_j$ ) with its respective weight ( $w_j$ ) and summing up all weighted models:

$$\phi = \sum w_j p_j \quad (E12)$$

### 3.6 Model uncertainty

To assess model uncertainty, we calculate 1) estimated data covariance matrix  $\hat{C}_d$ , 2) estimated model parameter covariance matrix  $\hat{C}_m$  (the variances of each parameter), and 3) model variance,  $\hat{\sigma}^2$ :

$$\hat{C}_d = \hat{\alpha} \tilde{C}_d \quad (E13)$$

$$\hat{C}_m = (G^T \hat{C}_d^{-1} G)^{-1} \quad (E14)$$

$$\hat{\sigma}_{i,j}^2 = q_i(t_j)^T \hat{C}_m^{-1} q_i(t_j) \quad (E15)$$

Where  $q_i(t_j)$  are the environmental variables at any given time. A 95% confidence interval was estimated from a two tailed Student's t-distribution for seven degrees of freedom multiplied by  $\hat{\sigma}$ . The final model is:

$$\hat{d}_{i,j} = \bar{d}_i + G_p \hat{m} \pm t\left(1 - \frac{\varepsilon}{2}, \nu\right) \hat{\sigma}_{i,j} \quad (E16)$$

Where  $\hat{d}_{i,j}$  are the predicted values for segment  $i$  for time  $j$ ,  $\bar{d}_i$  is the mean volume or width for segment  $i$ ,  $G_p$  is the system matrix of variables at times of interest (daily resolution),  $\hat{m}$  is the final model weighted average parameter vector, and  $t\left(1 - \frac{\varepsilon}{2}, \nu\right)$  is the two tailed Student's  $t$ -distribution.

## APPENDIX B: SUPPLEMENTARY FIGURES

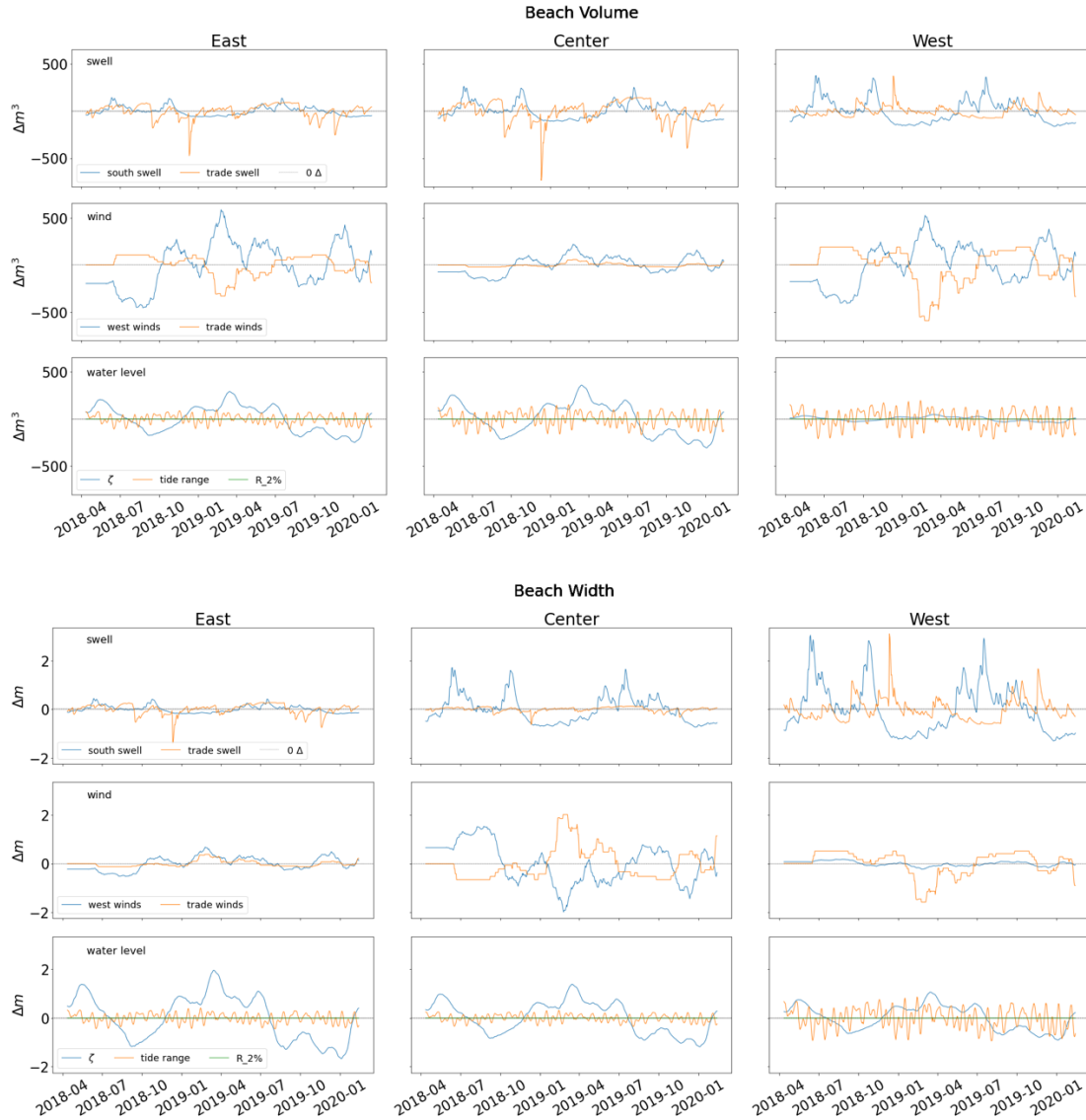


Figure S1. direction and magnitude of influence of environmental variables through time on beach volume (top) and width (bottom). Columns represent east, center, and west beach segments, and rows represent each group of physical variables. From the top: swell energy flux (south swell and trade-wind swell), wind characteristics (westerly winds and trade winds) and water level, including 30-day average water level ( $\zeta$ ), tide range, and run-up (R\_2%). For example, water levels (bottom plot, blue line), show a clear seasonal pattern for east; first contributing to accretion, then erosion by summer 2018, then accretion by winter, et cetera.

## APPENDIX C: SOURCES OF PHYSICAL ENVIRONMENTAL VARIABLES

- **Wave characteristics ( $H_s$ ,  $T$ ,  $\theta$ )** Cheung, K.F. 2010, updated 2014. Simulating WAVes Nearshore (SWAN) Regional Wave Model: O‘ahu. [February 2018 – February 2020] Distributed by the Pacific Islands Ocean Observing System (PacIOOS). [http://pacioos.org/metadata/swan\\_oahu.html](http://pacioos.org/metadata/swan_oahu.html). Accessed 10/03/2020
- **Ocean water level (historic, decadal, seasonal, hourly, daily)** Honolulu Station ID 1612340 station info: <https://tidesandcurrents.noaa.gov/stationhome.html?id=1612340>. Station data: P. C. Caldwell, M. A. Merrifield, P. R. Thompson (2015), Sea level measured by tide gauges from global oceans — the Joint Archive for Sea Level holdings (NCEI Accession 0019568), Version 5.5, NOAA National Centers for Environmental Information, Station 057. Dataset, doi:10.7289/V5V40S7W.
- **Wave energy flux (trade-wind waves)** Coastal Data Information Program (CDIP), M.A. McManus, M.A. Merrifield, and Pacific Islands Ocean Observing System (PacIOOS). 2000. PacIOOS Wave Buoy 098: Mōkapu Point, O‘ahu, Hawai‘i. January 2018 –to February 2020. Distributed by the Coastal Data Information Program (CDIP). <http://pacioos.org/metadata/cdip098.html>. Accessed 10/03/2020
- **Wave energy flux (South swell)** Coastal Data Information Program (CDIP), M.A. McManus, M.A. Merrifield, and Pacific Islands Ocean Observing System (PacIOOS). 2017. PacIOOS Wave Buoy 233: Pearl Harbor Entrance, O‘ahu, Hawai‘i. January 2018 – to February 2020. Distributed by the Coastal Data Information Program (CDIP). <http://pacioos.org/metadata/cdip233.html>. Accessed 10/03/2020
- **Wind speed and direction** National Centers for Environmental Information (NCEI). Climate Data Online. <https://www.ncdc.noaa.gov/cdo-web/>. Honolulu International Airport, HI, US. Station ID: GHCND:USW00022521 [January 2018 – February 2020] (Accessed 03/25/2021)
- **Run-up** M. Guiles, D. Luther, and M. Merrifield and Pacific Islands Ocean Observing System (PacIOOS), <http://www.pacioos.hawaii.edu/shoreline/runup-waikiki/>. Equations accessed 03/25/2021.

## REFERENCES

- Abessolo, G.O., Almar, R., Jouanno, J., Bonou, F., Castelle, B., Larson, M., 2020. Beach adaptation to intraseasonal sea level changes. *Environ. Res. Commun.* 2, 051003. <https://doi.org/10.1088/2515-7620/ab8705>
- Anderson, T.R., Frazer, L.N., Fletcher, C.H., 2010. Transient and persistent shoreline change from a storm. *Geophys. Res. Lett.* 37. <https://doi.org/10.1029/2009GL042252>
- Banno, M., Kuriyama, Y., 2020. Supermoon Drives Beach Morphological Changes in the Swash Zone. *Geophys. Res. Lett.* 47. <https://doi.org/10.1029/2020GL089745>
- Barbier, E.B., Hacker, S.D., Kennedy, C., Koch, E.W., Stier, A.C., Silliman, B.R., 2011. The value of estuarine and coastal ecosystem services. *Ecological Monographs* 81, 169–193. <https://doi.org/10.1890/10-1510.1>
- Bochicchio, C., Fletcher, C., Dyer, M., Smith, T., 2009. Reef-Top Sediment Bodies: Windward O‘ahu, Hawai‘i. *Pacific Science* 63, 61–82. [https://doi.org/10.2984/1534-6188\(2009\)63\[61:RSBWOH\]2.0.CO;2](https://doi.org/10.2984/1534-6188(2009)63[61:RSBWOH]2.0.CO;2)
- Booij, N., Ris, R.C., Holthuijsen, L.H., 1999. A third-generation wave model for coastal regions: 1. Model description and validation. *Journal of Geophysical Research: Oceans* 104, 7649–7666. <https://doi.org/10.1029/98JC02622>
- Burggraaff, O., Schmidt, N., Zamorano, J., Pauly, K., Pascual, S., Tapia, C., Spyrakos, E., Snik, F., 2019. Standardized spectral and radiometric calibration of consumer cameras. *Opt. Express*, OE 27, 19075–19101. <https://doi.org/10.1364/OE.27.019075>
- Cai, W., Borlace, S., Lengaigne, M., van Rensch, P., Collins, M., Vecchi, G., Timmermann, A., Santoso, A., McPhaden, M.J., Wu, L., England, M.H., Wang, G., Guilyardi, E., Jin, F.-F., 2014. Increasing frequency of extreme El Niño events due to greenhouse warming. *Nature Clim Change* 4, 111–116. <https://doi.org/10.1038/nclimate2100>
- Cai, W., Wang, G., Santoso, A., McPhaden, M.J., Wu, L., Jin, F.-F., Timmermann, A., Collins, M., Vecchi, G., Lengaigne, M., England, M.H., Dommenges, D., Takahashi, K., Guilyardi, E., 2015. Increased frequency of extreme La Niña events under greenhouse warming. *Nature Clim Change* 5, 132–137. <https://doi.org/10.1038/nclimate2492>
- Caldwell, P.C., Merrifield, M.A., Thompson, P.R., 2015. Sea level measured by tide gauges from global oceans — the Joint Archive for Sea Level holdings (NCEI Accession 0019568), Version 5.5, NOAA National Centers for Environmental Information, Dataset, [doi:10.7289/V5V40S7W](https://doi.org/10.7289/V5V40S7W).
- Conger, C.L., Fletcher, C.H., Barbee, M., 2005. Artificial Neural Network Classification of Sand in all Visible Submarine and Subaerial Regions of a Digital Image. *Journal of Coastal Research* 216, 1173–1177. <https://doi.org/10.2112/03-0099.1>
- Conger, C.L., Fletcher, C.H., Hochberg, E.H., Frazer, N., Rooney, J.J.B., 2009. Remote sensing of sand distribution patterns across an insular shelf: Oahu, Hawaii. *Marine Geology* 267, 175–190. <https://doi.org/10.1016/j.margeo.2009.10.005>
- Dail, H.J., Merrifield, M.A., Bevis, M., 2000. Steep beach morphology changes due to energetic wave forcing. *Marine Geology* 162, 443–458. [https://doi.org/10.1016/S0025-3227\(99\)00072-9](https://doi.org/10.1016/S0025-3227(99)00072-9)
- Devlin, A.T., Jay, D.A., Talke, S.A., Zaron, E.D., Pan, J., Lin, H., 2017. Coupling of sea level and tidal range changes, with implications for future water levels. *Sci Rep* 7, 17021. <https://doi.org/10.1038/s41598-017-17056-z>

- Doukari, M., Batsaris, M., Papakonstantinou, A., Topouzelis, K., 2019. A Protocol for Aerial Survey in Coastal Areas Using UAS. *Remote Sensing* 11, 1913. <https://doi.org/10.3390/rs11161913>
- El Mrini, A., Anthony, E.J., Maanan, M., Taaouati, M., Nachite, D., 2012. Beach-dune degradation in a Mediterranean context of strong development pressures, and the missing integrated management perspective. *Ocean & Coastal Management* 69, 299–306. <https://doi.org/10.1016/j.ocecoaman.2012.08.004>
- Firing, Y.L., Merrifield, M.A., 2004. Extreme sea level events at Hawaii: Influence of mesoscale eddies. *Geophysical Research Letters* 31. <https://doi.org/10.1029/2004GL021539>
- Fletcher, C., Rooney, J., Barbee, M., Lim, S., Richmond, B., 2003. Mapping Shoreline Change Using Digital Orthophotogrammetry on Maui, Hawaii. *Journal of Coastal Research* 106–124.
- Fletcher, C.H., Bochicchio, C., Conger, C.L., Engels, M.S., Feirstein, E.J., Frazer, N., Glenn, C.R., Grigg, R.W., Grossman, E.E., Harney, J.N., Isoun, E., Murray-Wallace, C.V., Rooney, J.J., Rubin, K.H., Sherman, C.E., Vitousek, S., 2008. Geology of Hawaii Reefs, in: Riegl, B.M., Dodge, R.E. (Eds.), *Coral Reefs of the USA*. Springer Netherlands, Dordrecht, pp. 435–487. [https://doi.org/10.1007/978-1-4020-6847-8\\_11](https://doi.org/10.1007/978-1-4020-6847-8_11)
- Frazer, L.N., Anderson, T.R., Fletcher, C.H., 2009. Modeling storms improves estimates of long-term shoreline change. *Geophys. Res. Lett.* 36, L20404. <https://doi.org/10.1029/2009GL040061>
- Garza, J.A., Chu, P.-S., Norton, C.W., Schroeder, T.A., 2012. Changes of the prevailing trade winds over the islands of Hawaii and the North Pacific: TRADE WIND CHANGES. *J. Geophys. Res.* 117, n/a-n/a. <https://doi.org/10.1029/2011JD016888>
- Grady, A.E., Moore, L.J., Storlazzi, C.D., Elias, E., Reidenbach, M.A., 2013. The influence of sea level rise and changes in fringing reef morphology on gradients in alongshore sediment transport. *Geophys. Res. Lett.* 40, 3096–3101. <https://doi.org/10.1002/grl.50577>
- Grossman, E.E., Barnhardt, W.A., Hart, P., Richmond, B.M., Field, M.E., 2006. Shelf stratigraphy and the influence of antecedent substrate on Holocene reef development, south Oahu, Hawaii. *Marine Geology* 226, 97–114. <https://doi.org/10.1016/j.margeo.2005.09.012>
- Habel, S., Fletcher, C.H., Barbee, M., Anderson, T.R., 2016. The influence of seasonal patterns on a beach nourishment project in a complex reef environment. *Coastal Engineering* 116, 67–76. <https://doi.org/10.1016/j.coastaleng.2016.06.006>
- Harney, J.N., Fletcher, C.H., 2003. A Budget of Carbonate Framework and Sediment Production, Kailua Bay, Oahu, Hawaii. *Journal of Sedimentary Research* 73, 856–868. <https://doi.org/10.1306/051503730856>
- Hino, M., Belanger, S.T., Field, C.B., Davies, A.R., Mach, K.J., 2019. High-tide flooding disrupts local economic activity. *Sci. Adv.* 5, eaau2736. <https://doi.org/10.1126/sciadv.aau2736>
- Hoegh-Guldberg, O., Mumby, P.J., Hooten, A.J., Steneck, R.S., Greenfield, P., Gomez, E., Harvell, C.D., Sale, P.F., Edwards, A.J., Caldeira, K., Knowlton, N., Eakin, C.M., Iglesias-Prieto, R., Muthiga, N., Bradbury, R.H., Dubi, A., Hatziolos, M.E., 2007. Coral Reefs Under Rapid Climate Change and Ocean Acidification. *Science* 318, 1737–1742. <https://doi.org/10.1126/science.1152509>

- Homer, P.S., 1964. Characteristics of deep water waves in Oahu area for a typical year, Prepared for the Board of Harbor Commissioners, State of Hawaii. Contract No. 5772. Marine Advisors, La Jolla, California.
- Houston, J.R., 2008. The economic value of beaches – A 2008 update. *Shore & Beach* 76, 22–26.
- IPCC, 2021. Summary for Policymakers. In: *Climate Change 2021: The Physical Science Basis. Contribution of Working Group I to the Sixth Assessment Report of the Intergovernmental Panel on Climate Change* [Masson-Delmotte, V., P. Zhai, A. Pirani, S. L. Connors, C. Péan, S. Berger, N. Caud, Y. Chen, L. Goldfarb, M. I. Gomis, M. Huang, K. Leitzell, E. Lonnoy, J.B.R. Matthews, T. K. Maycock, T. Waterfield, O. Yelekçi, R. Yu and B. Zhou (eds.)]. Cambridge University Press. In Press.
- Isoun, E., Fletcher, C., Frazer, N., Gradie, J., 2003. Multi-spectral mapping of reef bathymetry and coral cover; Kailua Bay, Hawaii. *Coral Reefs* 22, 68–82.  
<https://doi.org/10.1007/s00338-003-0287-4>
- Jeanson, M., Anthony, E.J., Dolique, F., Aubry, A., 2013. Wave characteristics and morphological variations of pocket beaches in a coral reef–lagoon setting, Mayotte Island, Indian Ocean. *Geomorphology* 182, 190–209.  
<https://doi.org/10.1016/j.geomorph.2012.11.013>
- Johnson, N.C., Feldstein, S.B., Tremblay, B., 2008. The Continuum of Northern Hemisphere Teleconnection Patterns and a Description of the NAO Shift with the Use of Self-Organizing Maps. *Journal of Climate* 21, 6354–6371.  
<https://doi.org/10.1175/2008JCLI2380.1>
- Knutson, T., Camargo, S.J., Chan, J.C.L., Emanuel, K., Ho, C.-H., Kossin, J., Mohapatra, M., Satoh, M., Sugi, M., Walsh, K., Wu, L., 2020. Tropical Cyclones and Climate Change Assessment: Part II: Projected Response to Anthropogenic Warming. *Bulletin of the American Meteorological Society* 101, E303–E322. <https://doi.org/10.1175/BAMS-D-18-0194.1>
- Kohonen, T., 1990. The self-organizing map. *Proceedings of the IEEE* 78, 1464–1480.  
<https://doi.org/10.1109/5.58325>
- Li, N., Cheung, K.F., Stopa, J.E., Hsiao, F., Chen, Y.-L., Vega, L., Cross, P., 2016. Thirty-four years of Hawaii wave hindcast from downscaling of climate forecast system reanalysis. *Ocean Modelling* 100, 78–95. <https://doi.org/10.1016/j.ocemod.2016.02.001>
- Liu, Y., Weisberg, R.H., Mooers, C.N.K., 2006. Performance evaluation of the self-organizing map for feature extraction. *J. Geophys. Res.* 111, C05018.  
<https://doi.org/10.1029/2005JC003117>
- Long, X., Widlansky, M.J., Schloesser, F., Thompson, P.R., Annamalai, H., Merrifield, M.A., Yoon, H., 2020. Higher Sea Levels at Hawaii Caused by Strong El Niño and Weak Trade Winds. *Journal of Climate* 33, 3037–3059. <https://doi.org/10.1175/JCLI-D-19-0221.1>
- Miller, T., Fletcher, C., 2003. Waikiki: Historical analysis of an engineered shoreline. *Journal of Coastal Research* 19, 1026–1043.
- NOAA, 2020. National Oceanic and Atmospheric Administration (2020). Tides & Currents. Tide Station 1612340 Station Info [WWW Document]. URL <http://tidesandcurrents.noaa.gov/inventory.html?id/41612340> (accessed 7.20.20).
- Norcross, Z., Fletcher, C., Rooney, J., Eversole, D., Miller, T., 2003. Hawaiian Beaches Dominated by Longshore Transport.

- Norcross, Z.M., Fletcher, C.H., Merrifield, M., 2002. Annual and interannual changes on a reef-fringed pocket beach: Kailua Bay, Hawaii. *Marine Geology* 190, 553–580.  
[https://doi.org/10.1016/S0025-3227\(02\)00481-4](https://doi.org/10.1016/S0025-3227(02)00481-4)
- Oppenheimer, M., Glavovic, B.C., Hinkel, J., van de Wal, R., Magnan, A.K., Abd-Elgawad, A., Cai, R., Cifuentes-Jara, M., Rica, C., DeConto, R.M., Ghosh, T., Hay, J., Islands, C., Isla, F., Marzeion, B., Meyssignac, B., Sebesvari, Z., Biesbroek, R., Buchanan, M.K., de Campos, R.S., Cozannet, G.L., Domingues, C., Dangendorf, S., Döll, P., Duvat, V.K.E., Edwards, T., Ekaykin, A., Frederikse, T., Gattuso, J.-P., Kopp, R., Lambert, E., Lawrence, J., Narayan, S., Nicholls, R.J., Renaud, F., Simm, J., Smit, A., Woodruff, J., Wong, P.P., Xian, S., Abe-Ouchi, A., Gupta, K., Pereira, J., 2019. Sea Level Rise and Implications for Low-Lying Islands, Coasts and Communities (IPCC Special Report on the Ocean and Cryosphere in a Changing Climate).
- PacIOOS, 2021a. Simulating Waves Nearshore (SWAN) Regional Wave Model: Oahu. Metadata [WWW Document]. URL  
[https://www.pacioos.hawaii.edu/metadata/swan\\_oahu.html](https://www.pacioos.hawaii.edu/metadata/swan_oahu.html) (accessed 2.1.21).
- PacIOOS, 2021b. Pacific Islands Ocean Observing System (PacIOOS). Wave Run-Up Forecast: Waikīkī, O‘ahu (about) [WWW Document]. URL  
<https://www.pacioos.hawaii.edu/shoreline/runup-waikiki/#about> (accessed 2.1.21).
- Pandolfi, J.M., Connolly, S.R., Marshall, D.J., Cohen, A.L., 2011. Projecting Coral Reef Futures Under Global Warming and Ocean Acidification. *Science* 333, 418–422.  
<https://doi.org/10.1126/science.1204794>
- Parsons, L.A., Coats, S., 2019. Ocean-Atmosphere Trajectories of Extended Drought in Southwestern North America. *J. Geophys. Res. Atmos.* 124, 8953–8971.  
<https://doi.org/10.1029/2019JD030424>
- Parsons, L.A., Coats, S., Overpeck, J.T., 2018. The Continuum of Drought in Southwestern North America. *J. Climate* 31, 8627–8643. <https://doi.org/10.1175/JCLI-D-18-0010.1>
- Potemra, J.T., Lukas, R., 1999. Seasonal to interannual modes of sea level variability in the western Pacific and eastern Indian oceans. *Geophysical Research Letters* 26, 365–368.  
<https://doi.org/10.1029/1998GL900280>
- Reusch, D.B., Alley, R.B., Hewitson, B.C., 2005. Relative Performance of Self-Organizing Maps and Principal Component Analysis in Pattern Extraction from Synthetic Climatological Data. *Polar Geography* 29, 188–212. <https://doi.org/10.1080/789610199>
- Risandi, J., Hansen, J.E., Lowe, R.J., Rijnsdorp, D.P., 2020. Shoreline Variability at a Reef-Fringed Pocket Beach. *Front. Mar. Sci.* 7. <https://doi.org/10.3389/fmars.2020.00445>
- Segura, L.E., Hansen, J.E., Lowe, R.J., 2018. Seasonal Shoreline Variability Induced by Subtidal Water Level Fluctuations at Reef-Fringed Beaches. *J. Geophys. Res. Earth Surf.* 123, 433–447. <https://doi.org/10.1002/2017JF004385>
- Stevenson, S., Wittenberg, A.T., Fasullo, J., Coats, S., Otto-Bliesner, B., 2021. Understanding Diverse Model Projections of Future Extreme El Niño. *Journal of Climate* 34, 449–464.  
<https://doi.org/10.1175/JCLI-D-19-0969.1>
- Tarui, N., Peng, M., Eversole, D., 2018. Economic Impact Analysis of the Potential Erosion of Waikīkī Beach. A 2016 Update. University of Hawai‘i Sea Grant College Program.
- Theuerkauf, E.J., Rodriguez, A.B., Fegley, S.R., Luettich, R.A., 2014. Sea level anomalies exacerbate beach erosion. *Geophys. Res. Lett.* 41, 5139–5147.  
<https://doi.org/10.1002/2014GL060544>

- Thompson, P.R., Widlansky, M.J., Hamlington, B.D., Merrifield, M.A., Marra, J.J., Mitchum, G.T., Sweet, W., 2021. Rapid increases and extreme months in projections of United States high-tide flooding. *Nat. Clim. Chang.* 11, 584–590. <https://doi.org/10.1038/s41558-021-01077-8>
- Thompson, P.R., Widlansky, M.J., Merrifield, M.A., Becker, J.M., Marra, J.J., 2019. A Statistical Model for Frequency of Coastal Flooding in Honolulu, Hawaii, During the 21st Century. *J. Geophys. Res. Oceans* 124, 2787–2802. <https://doi.org/10.1029/2018JC014741>
- USGS, 2017a. Agisoft Photoscan Workflow. United States Geological Survey [WWW Document]. URL <https://uas.usgs.gov/nupo/pdf/USGSAgisoftPhotoScanWorkflow.pdf> (accessed 2.1.19).
- USGS, 2017b. Unmanned Aircraft Systems Post Processing; Structure-from-motion photogrammetry. United States Geological Survey. March 2017 [WWW Document]. URL <https://uas.usgs.gov/nupo/pdf/PhotoScanProcessingDSLRLMar2017.pdf> (accessed 2.1.19).
- Vitousek, S., Fletcher, C.H., 2008. Maximum Annually Recurring Wave Heights in Hawai‘i. *Pacific Science* 62, 541–553. [https://doi.org/10.2984/1534-6188\(2008\)62\[541:MARWHI\]2.0.CO;2](https://doi.org/10.2984/1534-6188(2008)62[541:MARWHI]2.0.CO;2)
- Widlansky, M.J., Long, X., Schloesser, F., 2020. Increase in sea level variability with ocean warming associated with the nonlinear thermal expansion of seawater. *Commun Earth Environ* 1, 1–12. <https://doi.org/10.1038/s43247-020-0008-8>
- Wiegel, R.L., 2008. Waikiki Beach, Oahu, Hawaii: History of its transformation from a natural to an urban shore. *Shore & Beach* 76, 28.
- Wright, L.D., Short, A.D., 1984. Morphodynamic variability of surf zones and beaches: A synthesis. *Marine Geology* 56, 93–118.